
Numerical study on a heat-driven piston-coupled multi-stage thermoacoustic-Stirling cooler

Jingyuan Xu^{a,d*}, Jianying Hu^{b*}, Ercang Luo^{b,c}, Jiangfeng Hu^{b,c}, Limin Zhang^b, Simone Hochgreb^d

a. Department of Chemical Engineering, Imperial College London, London SW7 2BU, United Kingdom

b. CAS Key Laboratory of Cryogenics, Technical Institute of Physics and Chemistry, Chinese Academy of Sciences, Beijing 100190, China

c. University of Chinese Academy of Sciences, Beijing 100049, China

d. Department of Engineering, University of Cambridge, Cambridge CB2 1PZ, United Kingdom

Abstract

This work investigates a novel heat-driven multi-stage thermoacoustic cooler that can satisfy cooling requirements in the applications of natural gas liquefaction and high-temperature superconductivity. The proposed system consists of a compressor, multiple thermoacoustic units (engines and coolers) coupled by piston-cylinder assemblies. The acoustic power input by the compressor is successively multiplied in the thermoacoustic engine units, and the amplified acoustic power is then consumed to produce cooling power in the thermoacoustic cooler units. The proposed system overcomes the limitations of the traditional thermoacoustic systems owing to high efficiency, compact size, and ease of control. Analyses are first performed to explore the influence of the number of stages. The design method of the pistons is presented based on acoustic impedance matching principle. Based on the optimized system, simulations are then conducted to investigate the axial distribution of the key parameters, which can explain the reason for improved thermodynamic performance. At heating and cooling temperatures of 873 K and 130 K, the system achieves a cooling power of 2.1 kW and a thermal-to-cooling relative Carnot efficiency of 23%. This represents significant increases by over 60% in efficiency and 80% in cooling capacity when compared to existing systems. Simulations further demonstrate how controlling the input acoustic power and frequency via the compressor enables control of the system under various conditions. Further discussions are made considering a potential combined cooling and power system, indicating a thermal-cooling-electricity efficiency of 34% without any external electric power required for the compressor.

* Corresponding author. Tel/Fax: +44 7422 527596 E-mail: jingyuan.xu@imperial.ac.uk (JY Xu)
Tel/Fax: +86 10 82543733 E-mail: jyhu@mail.ipc.ac.cn (JY Hu)

Keywords

Thermoacoustic; Stirling; Cooler; Engine; Heat driven; Combined cooling and power (CCP)

Nomenclature

Symbols

A	area, m ²
c	scale factor
C_e	electrical capacitance, F
d_h	hydraulic diameter, m
D	diameter, m
f	frequency, Hz
K_m	mechanical spring stiffness, N/m
K_g	gas spring stiffness, N/m
K_{tot}	total spring stiffness, N/m
L_e	electrical inductance, H
M	number of cooler stages
M	moving mass of piston, kg
N	number of engine stages
P	pressure, Pa
$Q_{h,n}$	input thermal power at the n^{th} stage of the engine, W
$Q_{c,m}$	cooling power obtained at the m^{th} stage of cooler, W
$Q_{h,all}$	overall input thermal power, W
$Q_{c,all}$	overall cooling power, W
r_e	engine power factor
r_c	cooler power factor
R_m	mechanical damping, (N [■] s)/m
R_t	turbulent Reynolds number
$R_{e,in}$	internal electrical resistance, Ω
$R_{e,out}$	external electrical resistance, Ω
T	temperature, K
U	volume flow rate, m ³ /s
V	volume, m ³
V_a	Valensi number
W_0	input acoustic power from the compressor, W
W_{in}	acoustic impedance at the inlet of the component, W
W_{out}	acoustic impedance at the outlet of the component, W
$W_{c,in}$	acoustic power at the inlet of the first-stage cooler unit, W
W_{elec}	electric power, W

X	amplitude of displacement, m
$ Z $	amplitude of acoustic impedance, Pa \cdot s /m ³

Greek letters

η_e	efficiency of an engine unit
η_c	efficiency of a cooler unit
η_p	efficiency of a piston
η_{eng}	efficiency of a multi-stage engine
η_{col}	efficiency of a multi-stage cooler
η_{alt}	efficiency of an alternator
$\eta_{ove,sys}$	overall system efficiency
$\eta_{tc,sys}$	thermal-to-cooling system efficiency
$\eta_{tce,sys}$	thermal-cooling-electricity system efficiency
θ	phase of acoustic impedance, $^\circ$
ω	angular frequency, rad/s
ε	average height of surface irregularities
ϕ	porosity
τ	transduction coefficient, N/A
$ $	numerical value of

Subscripts

0	ambient
1	first order
b	back space
c	cold
com	compression-side
p	piston
exp	expansion-side
f	front
h	heating
m	mean

1 Introduction

Small-scale cryogenic coolers that can deliver a few hundred watts to kilowatts of cooling power at liquid nitrogen to liquid natural gas temperatures (77 K~130 K) are essential for several applications. These are typically used for high-temperature superconducting electric power [1,2], which includes fault current limiters, transformers, motors, generators, and superconducting magnetic energy storage magnets. These high-temperature superconducting applications may require a few hundred watts of cooling power at nitrogen liquefaction temperature ranges [3,4]. Liquefaction of unconventional natural gas extracted from remote areas is another area for such coolers [5-6], where pipeline transport is inaccessible or uneconomical. The typically required cooling power in those cases is a few kilowatts at natural gas liquefaction temperatures.

Thermoacoustically-driven coolers can be good candidates to satisfy such demands. These coolers use high-amplitude acoustic waves to pump heat from the cold load to the hot sink using acoustic work provided by an integrated thermoacoustic engine [7,8]. Cooling based on such thermodynamic cycles involves no harmful ozone-depleting gases, no mechanical moving parts, and no electric power. Many efforts have been made to develop the thermoacoustically-driven coolers at cryogenic operating temperatures. In 1990, a thermoacoustically-driven cooler was first developed by Radebaugh *et al.* using a standing-wave thermoacoustic engine as a prime mover and a cooling temperature of 90 K was achieved [9]. In 1997, Praxair in conjunction with Los Alamos National Laboratory developed a large-scale thermoacoustically-driven cooler for natural gas liquefaction. The system obtained a cooling power of 2.1 kW at 125 K with a relative Carnot efficiency of 5.8 % [10]. In 1999, Backhaus and Swift demonstrated a traveling-wave thermoacoustic engine that achieved a high thermal efficiency of 30% [11]. Based on this configuration, most subsequent research on thermoacoustically-driven coolers aimed to achieve lower cooling temperatures, reducing the cooling temperature to liquid nitrogen temperatures (~80 K) [12-14], and even, to liquid hydrogen temperatures (~20 K) [15]. However, the non-compact size caused by the large-diameter standing-wave resonance tubes in this thermoacoustic engine have hindered its use in many applications. To solve this problem, in 2010, de Blok proposed a looped multi-stage thermoacoustic engine that reduced the system volume by a factor of 5 [16]. This type of thermoacoustic engine has been widely used for most subsequent work for low-grade heat recovery [17,18], natural gas liquefaction [19], cryogenic cooling [20] and refrigeration [21]. In 2012, de Blok further developed a looped thermoacoustically-driven cooler [22]. The system achieved a measured relative Carnot efficiency of 6.7% and a cooling power of 95 W at a cooling temperature of 227 K. In 2015, Zhang *et al.* developed a looped three-stage thermoacoustically-driven cooler which couples a cooler unit at each branch of an engine unit [23]. They experimentally achieved a relative Carnot efficiency of 8% and a cooling power of 1.2 kW at a cooling temperature of 130 K. In 2019, Xu *et al.* developed a looped three-

stage thermoacoustically-driven cooler by using different diameter resonance tubes for matching acoustic impedances [24]. The experimental results show that the system achieved a relative Carnot efficiency of 10% and a cooling power of 378 W at a cooling temperature of 130 K [25].

While several breakthroughs have been recently reported in the current thermoacoustically-driven coolers from the literature review, existing thermoacoustic systems have still shown three key limitations. The first limitation is the low cooling efficiency arising from poor phase-shifting capability and large power loss in the current resonance tubes; the former makes it difficult to obtain the optimal acoustic fields for thermoacoustic units, and the latter takes a large portion of the available energy. The second limitation is the poor power density owing to the non-compact resonance tubes. The third limitation is the slow control of the system operating state with long thermal response time, due to the significant thermal response hysteresis in regenerators and heat exchangers.

To this end, a thermoacoustically-driven cooler that has high efficiency, high power density and easy control, is highly required, which, however, is still lacking from previous work. This paper aims to fill this knowledge gap and to investigate a thermoacoustically-driven cooler that can overcome the above limitations of the existing systems by:

(i) introducing pistons to replace long resonance tubes to couple the thermoacoustic energy-conversion units, i.e., the engine and cooler units: this improves efficiency due to the lower power losses and better phase-shifting capability of the piston, and increases power density due to the reduced size of the piston;

(ii) using a cascade arrangement of the cooler which further contributes to the high efficiency due to power recovery;

(iii) employing a linear compressor at the inlet of the system, which enables a very short system response to working frequency and input power demand.

To the best of the authors' knowledge, no studies were found on investigating of such thermoacoustically-driven cooler and its variant. The proposed configuration, therefore, leads to a new generation of a thermoacoustically-driven cooler that is highly efficient, compact, and easy to control. A detailed theoretical analysis of a cooling-only system is presented first, followed by a discussion on a potentially improved combined cooling and power system.

2. System Configuration

Figure 1 shows a schematic of the proposed thermoacoustically-driven cooler. It includes a compressor, three thermoacoustic engine units, two thermoacoustic cooler units, four piston-cylinder assemblies and a phase shifter assembly (inertance tube and gas reservoir). A compressor is located at one end of the system. Multiple thermoacoustic units are coupled by using the coupled pistons to modulate the acoustic fields. An exception is made for the final cooler stage, where an inertance tube and a

gas reservoir are used as the phase shifter. Figure 2 shows a close-up view of the piston-cylinder assembly, which is composed of an expansion space, an expansion-side piston, a compression-side piston, mechanical springs, and a compression space, as usually used in Stirling engines [26,27] and coolers [28]. The feasibility of using such pistons for coupling has been verified by Hu *et al.* in their thermoacoustic engine [29]. Each thermoacoustic engine unit consists of a water-cooler, a regenerator, and a heater; the engine unit converts thermal energy into acoustic power when a temperature gradient is applied along with the regenerator. Each thermoacoustic cooler unit consists of two water-coolers, a regenerator, a cold-head, and a pulse tube; the cooler unit uses the acoustic power to pump heat from the cold side to the ambient side, thus generating a temperature gradient along with the regenerator. The working principles of the overall system are as follows: the electrically-driven compressor provides input acoustic power to the 1st engine unit; acoustic power is then successively amplified in the multiple engine units; the final amplified acoustic power is then consumed successively in each cooler unit to obtain cooling power; the remaining power is dissipated as heat in the inductance tube.

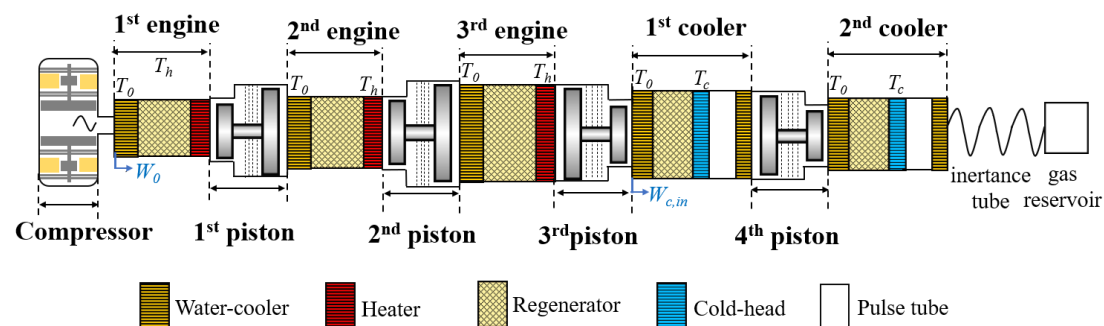


Figure 1. A piston-coupled cascade multi-stage thermoacoustically-driven cooler (taking a system with a 3-stage engine and a 2-stage cooler as an example).

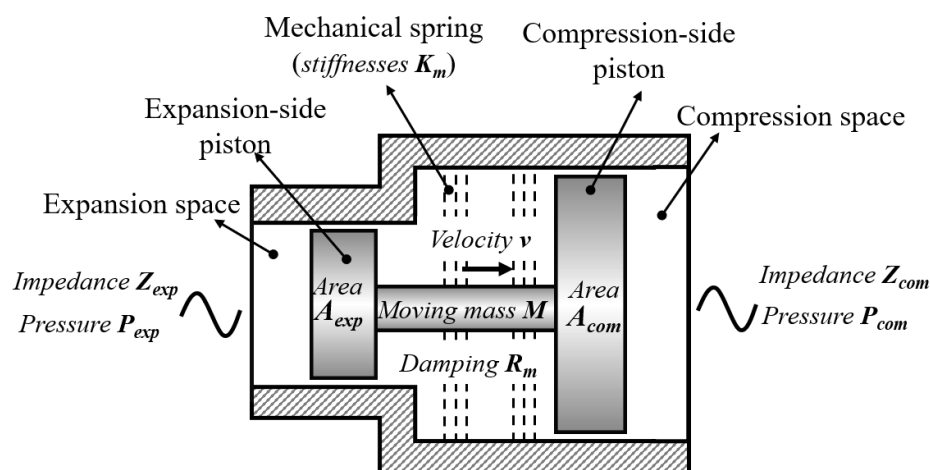


Figure 2. Enlarged view of the piston-cylinder assembly

As demonstrated further on, the proposed system has several advantages when compared to the existing thermoacoustically-driven coolers: high efficiency, which is increased by lower power loss and accurate phase shift capability of the piston relatively

to a resonance tube; compact size, because of the much-reduced length of the pistons compared to the resonance tubes; ease of control, achieved by using a compressor to actively modulate the system operating state with short response. Finally, the cascade arrangement of the engine allows for both the customization of the cooling power, and high efficiency via the cascade arrangement of the cooler due to power recovery.

All thermoacoustic engine units have identical heating temperature T_h and thermoacoustic cooler units have identical cooling temperatures T_c . We define the input acoustic power from the compressor as W_0 , the input thermal power at the n^{th} stage of the engine as $Q_{h,n}$, the cooling power obtained at the m^{th} stage of cooler as $Q_{c,m}$, the number of the stage of the engine as N , and the number of stages of the cooler as M . Here we focus only on the performance of the cooler, so the efficiency of the compressor is not considered. In the proposed system, there are two types of input power contributing to cooling power, i.e., input acoustic power from the compressor W_0 and input thermal energy $Q_{h,n}$. Two types of relative Carnot efficiencies for the system are defined as: (1) an overall system efficiency $\eta_{ove,sys}$ that considers the contributions of both input powers from the compressor and thermal source; (2) a thermal-to-cooling system efficiency $\eta_{tc,sys}$ that excludes the contribution of input powers from the compressor (i.e., W_0) and only considers the contribution of input thermal energy, particularly for heat-driven type cooling systems. The efficiencies $\eta_{ove,sys}$ and $\eta_{tc,sys}$ are expressed as

$$\eta_{ove,sys} = \frac{\left(\frac{T_0}{T_c} - 1\right) \sum_{m=1}^M Q_{c,m}}{\left(1 - \frac{T_0}{T_h}\right) \sum_{n=1}^N Q_{h,n} + W_0} \quad (1)$$

$$\eta_{tc,sys} = \frac{\left(1 - \frac{W_0}{W_{c,in}}\right) \left(\frac{T_0}{T_c} - 1\right) \sum_{m=1}^M Q_{c,m}}{\left(1 - \frac{T_0}{T_h}\right) \sum_{n=1}^N Q_{h,n}} \quad (2)$$

where $W_{c,in}$ is the acoustic power at the inlet of the first-stage cooler unit, which includes the input acoustic power from the compressor and the acoustic power amplified by thermoacoustic, as shown in Figure 1. The numerator of Eq. (1) corresponds to the overall cooling exergy, and the denominator includes both the exergy from the input thermal energy and input acoustic power from the compressor. The term $1 - W_0/W_{c,in}$ in Eq.(2) represents the fraction of the input thermal energy contributing to cooling. Therefore, the numerator of Eq. (2) only considers the fraction of the cooling exergy that is converted from the input thermal energy, and the denominator includes only the exergy from the input thermal energy.

3. Analysis of systems with different numbers of stages

In this section, analyses are conducted on the systems with different numbers of energy conversion stages, i.e., thermoacoustic engine and cooler. Because the optimum

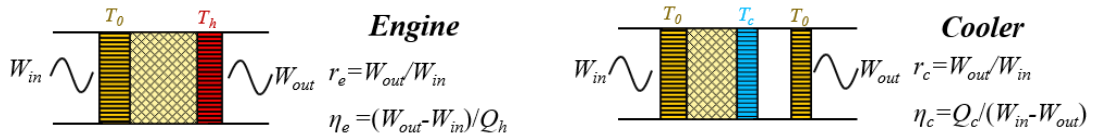
acoustic field in the regenerators can be realized by adjusting the phase of the coupled pistons, the thermoacoustic energy conversion unit displays similar temperature-dependent operating characteristics as that of Stirling engine/cooler. For each engine unit consisting of a water-cooler, a regenerator and a heater, we therefore assume that the power factor, $r_e = W_{out}/W_{in}$, and the engine efficiency, $\eta_e = (W_{out} - W_{in})/Q_h$, depend only on the hot and ambient temperatures when subject to optimal acoustic impedances at the boundaries, and is therefore the same for each engine unit. Likewise, for each cooler unit consisting of a water-cooler, a regenerator and a cold-head, each cooler power factor, $r_c = W_{out}/W_{in}$, and cooling efficiency $\eta_c = Q_c/(W_{in} - W_{out})$, should be the same under the optimal acoustic impedances. For different size of the energy conversion unit, the input power is directly proportional to the cross-sectional area of the regenerator, while the power factor and efficiency are approximately constant with scale. Other dimensions (e.g., length, porosity, channel width of the component, etc.) were chosen as typical geometries, and are outlined in Table 2. Figure 3 shows the simulation results of the general temperature-dependent performance for each thermoacoustic unit by using the Sage program [30] (see detailed introductions in Section 4.1). In each calculation, the acoustic impedances at the boundaries are optimized to achieve the highest efficiency. The simulations were made for the fixed parameters of input acoustic power of 2 kW and an ambient temperature of 293 K, whilst the hot and cold temperatures were varied. The resulting curves were fitted to first or second order polynomials involving only numerical value of absolute temperatures $|T_c|$ and $|T_h|$ for convenience. r_e , η_e , r_c and η_c are calculated as

$$r_e = 2.38 \times 10^{-3} |T_h| + 3 \times 10^{-2} \quad (3)$$

$$\eta_e = 1.78 \times 10^{-3} |T_h| - 8.19 \times 10^{-7} |T_h|^2 - 4.14 \times 10^{-1} \quad (4)$$

$$r_c = 2.16 \times 10^{-3} |T_c| + 2.72 \times 10^{-2} \quad (5)$$

$$\eta_c = 1.49 \times 10^{-3} |T_c| + 8.96 \times 10^{-6} |T_c|^2 - 2.56 \times 10^{-2} \quad (6)$$



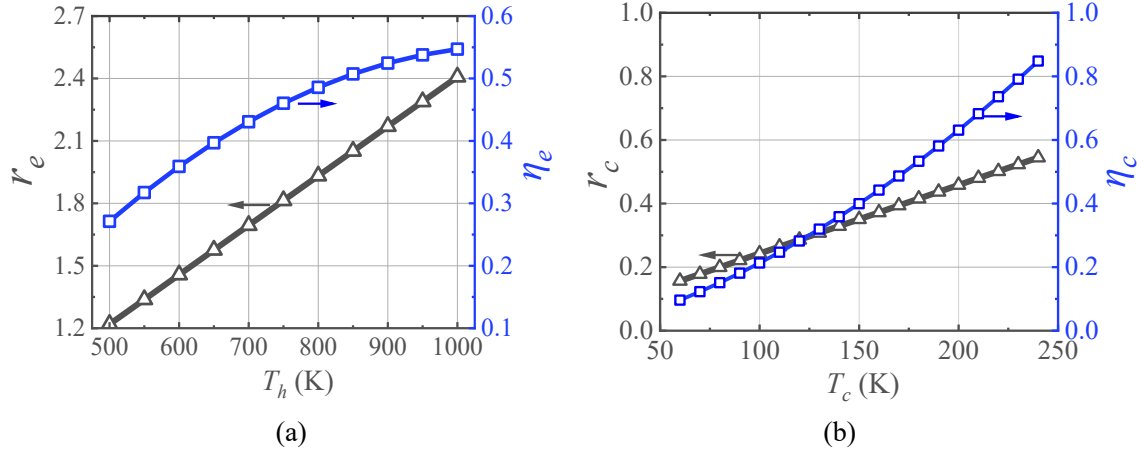


Figure 3. Power factors and efficiencies as a function of working temperatures for the (a) engine unit (b) cooler unit. Symbols are calculated point results, and lines are fits described in Eqs. (3)-(6).

The input thermal power at the n^{th} stage engine unit, $Q_{h,n}$, is therefore calculated as

$$Q_{h,n} = \frac{(r_e - 1)(r_e \eta_p)^{n-1} W_0}{\eta_e} \quad (7)$$

where η_p is the piston power transmission efficiency that is assumed to be the same for each piston.

The overall input thermal power, $Q_{h,all}$, is given by the sum of all input thermal power for N engine stages is given as,

$$Q_{h,all} = \sum_{n=1}^N Q_{h,n} = \frac{(1 - (r_e \eta_p)^N)(r_e - 1)W_0}{(1 - r_e \eta_p)\eta_e} \quad (8)$$

The acoustic power at the inlet of the first-stage cooler, $W_{c,in}$, is

$$W_{c,in} = (r_e \eta_p)^N W_0 \quad (9)$$

The cooling power obtained at the m^{th} stage cooler units, $Q_{c,m}$, is likewise calculated as

$$Q_{c,m} = \eta_c (1 - r_c)(r_c \eta_p)^{m-1} (r_e \eta_p)^N W_0 \quad (10)$$

The overall cooling power, $Q_{c,all}$, for M cooler stages is expressed as

$$Q_{c,all} = \sum_{m=1}^M Q_{c,m} = \frac{\eta_c (r_e \eta_p)^N (1 - r_c)(1 - (r_c \eta_p)^M)W_0}{1 - r_c \eta_p} \quad (11)$$

Taking Eqs. (8), (9) and (11) into Eqs. (1) and (2), $\eta_{ic,sys}$ and $\eta_{ove,sys}$ can be obtained as

$$\eta_{ic,sys} = \frac{\eta_c (r_e \eta_p)^N (1 - r_c)(1 - (r_c \eta_p)^M) \left(\frac{T_0}{T_c} - 1\right) \left(1 - \frac{1}{(r_e \eta_p)^N}\right) (1 - r_e \eta_p) \eta_e}{(1 - r_c \eta_p)(r_e - 1)(1 - (r_e \eta_p)^N) \left(1 - \frac{T_0}{T_h}\right)} \quad (12)$$

$$\eta_{ove,sys} = \frac{\eta_c (r_e \eta_p)^N (1 - r_c) (1 - (r_e \eta_p)^M) \left(\frac{T_0}{T_c} - 1\right)}{(1 - r_c \eta_p) \left[\frac{(1 - (r_e \eta_p)^N) (r_e - 1)}{(1 - r_e \eta_p) \eta_e} \left(1 - \frac{T_0}{T_h}\right) + 1 \right]} \quad (13)$$

Taking Eqs. (3) to (6) into Eqs. (12) and (13), together with Eq. (11), the influence of the number of engine stages, N , and number of cooler stages M on $\eta_{ove,sys}$, $\eta_{tc,sys}$ and $Q_{c,all}/W_0$ is shown in Figure 4. The assumed piston efficiency η_p was measured within the range between 0.83 to 0.88 [31], so η_p is set to be 0.85 in the following calculations. For a fixed number of cooler stages, increasing number of engine stages, N , decreases $\eta_{ove,sys}$ for $N < 4$, but the effect eventually tapers off. The increase in the number of engine stages has negligible impact on $\eta_{tc,sys}$ and results in higher $Q_{c,all}/W_0$. Likewise, for a fixed number of engine stages, an increase in the number of cooler stages, M , has a favorable effect on above two efficiencies up to 2, beyond which it is not too relevant. Taking $N=3$ as an example, $\eta_{tc,sys}$ and $\eta_{ove,sys}$ are increased by about 16% when the number of cooler stages increases from 1 to 2. Therefore, under the specific working conditions, a two-stage cooler unit is best for high efficiency.

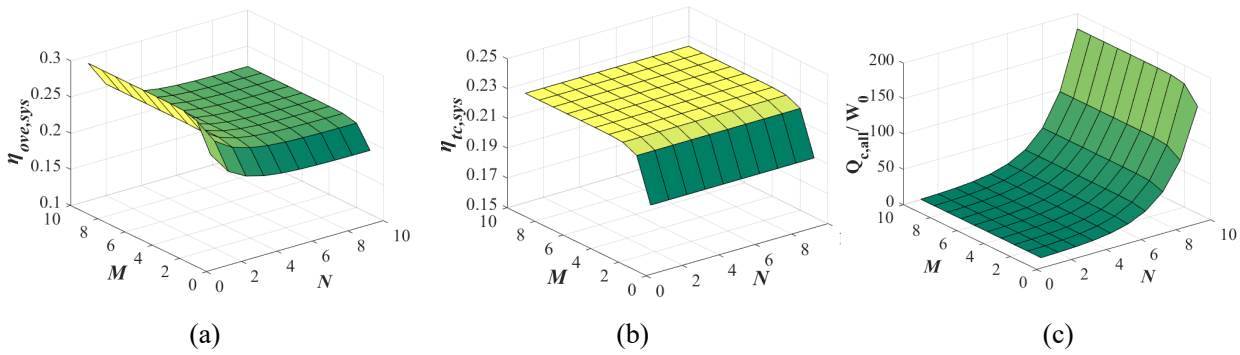


Figure 4. Influence of the number of engine stages, N , and cooler stages, M , on (a) optimal overall system efficiency $\eta_{ove,sys}$ (b) optimal thermal-to-cooling system efficiency $\eta_{tc,sys}$ and (c) cooling power ratio $Q_{c,all}/W_0$. T_h is 900 K, T_c is 70 K, T_0 is 300 K, η_p is 0.85.

Figure 5 shows the influence of the heating and cooling temperatures, T_h and T_c , on $\eta_{ove,sys}$, $\eta_{tc,sys}$ and $Q_{c,all}/W_0$ for $N=3$ and $M=3$. For a fixed cooling temperature, a higher value of heating temperature increases $\eta_{tc,sys}$ and $Q_{c,all}/W_0$, but has only a slight effect on the overall efficiency, $\eta_{ove,sys}$, because the denominator W_0 bears no relation to the working temperature. Yet for a fixed heating temperature, high values of cooling temperatures degrade the overall system performance. This is a result of the large cooler power factor r_c , which means that large acoustic power is wasted as heat in the final stage of the cooler unit. At heating and cooling temperatures of 900 K and 100 K, respectively, the system can achieve the highest $\eta_{tc,sys}$ of 22.8% and a peak $Q_{c,all}/W_0$ of 2.45.

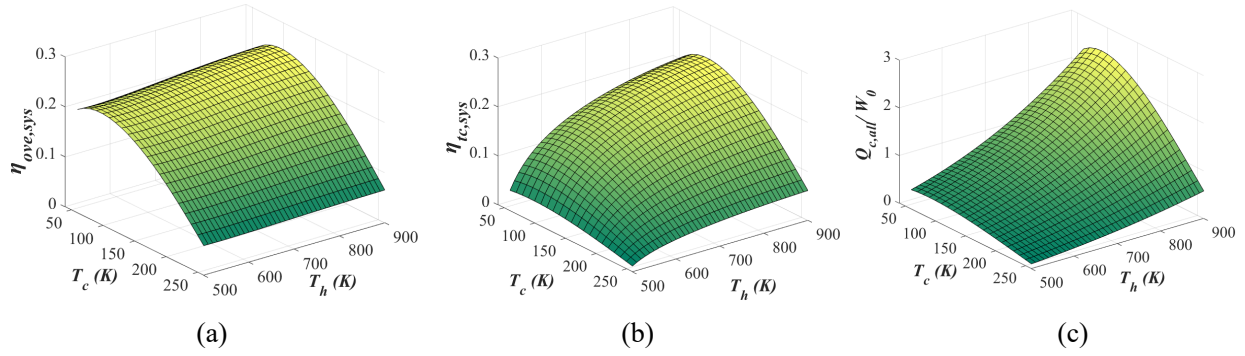


Figure 5. Influence of the heating temperature T_h and cooling temperature T_c on (a) optimal overall system efficiency $\eta_{ove,sys}$ (b) optimal thermal-to-cooling system efficiency $\eta_{tc,sys}$ and (c) cooling power ratio $Q_{c,all}/W_0$. N is 3, M is 3, T_0 is 300 K, η_p is 0.85.

According to the calculation results above, a system with a 3-stage engine and a 2-stage cooler is chosen for the following calculations, as it allows optimum power and high efficiency with a minimum number of stages.

4. Numerical simulations of the system operating characteristics

In this section, the operating characteristics of a typical system are investigated in detail by using the Sage program [30]. The numerical investigations focus on the system design, axial distributions of key parameters, thermodynamic performance as well as parametric sensitivity.

4.1 Simulation model

The Sage program solves for the steady operation of a thermoacoustic network of elements in the system according to parameter input values. The program consists of many model instances such as regenerators, heat exchangers, pistons, tubes and so on, each of which is a collection of component building blocks with parameter input values. The model instances are connected and assembled according to the geometric configuration to form an overall system. The program solves the equations for conservation of mass, momentum, and energy for each model instance. In the model, the governing equations of continuity, momentum, energy equations for the gas domain as well as the ideal gas equation of state are [32]:

$$\frac{\partial \rho A}{\partial t} + \frac{\partial \rho u A}{\partial x} = 0 \quad (14)$$

$$\frac{\partial \rho u A}{\partial t} + \frac{\partial u \rho u A}{\partial x} + \frac{\partial P}{\partial x} A - FA = 0 \quad (15)$$

$$\frac{\partial \rho e A}{\partial t} + P \frac{\partial A}{\partial t} + \frac{\partial}{\partial x} (u \rho e A + u P A + q) - Q_w = 0 \quad (16)$$

$$P = \rho R T \quad (17)$$

where P , u , A and ρ are the pressure wave, mean-flow velocity, cross section area and gas density, respectively, and R is the gas constant. The variable e is mass-specific total gas energy with $e=\kappa+u^2/2$ (κ is mass-specific internal gas energy). The factor F represents the viscous pressure gradient, Q_w is the heat flow per unit length due to heat transfer, and q is the conductive heat flow in the axial direction. Terms F , Q_w and q are formulated as [32]

$$F = -(f_D / d_h + K_{los} / l) \rho u |u| / 2 \quad (18)$$

$$Q_w = Nu(k / d_h) S_x (T_w - T) \quad (19)$$

$$q = -N_k k_g \frac{\partial T}{\partial x} A \quad (20)$$

where f_D , d_h and K_{los} are the Darcy friction factor, hydraulic diameter and total local loss coefficient respectively. Nu , k_g , S_x and $(T_w - T)$ are the Nusselt number, gas conductivity, wetted perimeter, and temperature difference between the negative z surface and section-average, respectively. N_k is an axial-conductivity enhancement ratio that is represented as a ratio of the effective gas conductivity to the molecular conductivity. Table 1 lists empirical terms f_D , Nu and N_k used in the simulation model for different types of components.

The force-balance equation of the piston is given as:

$$P_{exp} A_{exp} - P_{com} A_{com} - R_m v + i \frac{K_{tot}}{\omega} v = i \omega M v \quad (21)$$

where P is the pressure wave, A the piston area, M the total piston mass, K_{tot} the total spring stiffness of the piston which consists of mechanical spring stiffnesses K_m and gas spring stiffnesses K_g , R_m the mechanical damping of the piston, ω the angular frequency, v the velocity of the piston. Subscripts *exp* and *com* refer to the expansion-side and compression-side of the piston. All above parameters are presented in Figure 2. K_g is expressed as [31],

$$K_g = \frac{\gamma P_m A}{V_b} \quad (22)$$

where γ is the specific heat ratio, P_m is the mean pressure, and V_b is the volume of the back space of the piston-cylinder assembly.

The acoustic power is defined as

$$W = \frac{1}{2} |P_1| |U_1| \cos \theta \quad (23)$$

where θ is the phase difference between the pressure wave and the volume flow rate.

The acoustic impedance Z is given by

$$Z = \frac{P_1}{U_1} = \text{Re} \left[\frac{P_1}{U_1} \right] + i \text{Im} \left[\frac{P_1}{U_1} \right] \quad (24)$$

Table 1. Empirical terms of Darcy friction factor f_D , Nusselt number Nu , and axial-conductivity enhancement ratio N_k for different types of components in the simulation model [32]. Re , Pr and Pe are the Reynolds number, Prandtl number and Peclet number, respectively. Other symbols are defined in the nomenclature section.

Component	Type	f_D	Nu	N_k
Heat exchanger	Shell tube	Laminar: $f_D = \frac{64}{Re}$ Turbulent: $f_D = 0.11 \left(\frac{\varepsilon}{d_h} + \frac{68}{Re} \right)^{0.25}$	Laminar steady: $Nu = 6$ Turbulent: $Nu = 0.036 Re^{0.8} \left(\frac{l}{d_h} \right)^{-0.055} Pr^{0.33}$	Laminar: $N_k = 1$ Turbulent: $N_k = 0.022 Re^{0.75} Pr$
	Plate fin	Laminar: $f_D = \frac{96}{Re}$ Turbulent: $f_D = 0.11 \left(\frac{\varepsilon}{d_h} + \frac{68}{Re} \right)^{0.25}$	Laminar steady: $Nu = 10c$ Turbulent: $Nu = 0.035 Re^{0.75} Pr^{0.33}$	Laminar: $N_k = 1$ Turbulent: $N_k = 0.022 Re^{0.75} Pr$
Regenerator	Woven screen matrix	$f_D = \frac{129}{Re} + 2.91 Re^{-0.103}$	$Nu = (1 + 0.99 Pe^{0.66}) \phi^{1.79}$	$N_k = 1 + 0.5 Pe^{0.66} \phi^{-2.91}$
	Random fiber matrix	$f_D = \frac{a_1}{Re} + a_2 Re^{a_3}$ $(a_1 = 25.7 \left(\frac{\phi}{1-\phi} \right) + 79.8,$ $a_2 = 0.146 \left(\frac{\phi}{1-\phi} \right) + 3.76,$ $a_3 = -0.00283 \left(\frac{\phi}{1-\phi} \right) - 0.0748)$	$Nu = 1 + b_1 Pe^{b_2}$ $(b_1 = 0.186 \left(\frac{\phi}{1-\phi} \right),$ $b_2 = 0.55)$	$N_k = 1 + Pe^{0.55}$
	Packed sphere matrix	$f_D = \left(\frac{157}{Re} + 5.15 Re^{-0.137} \right) \left(\frac{\phi}{0.39} \right)^{3.48}$	$Nu = 1 + 0.48 Pe^{0.65}$	$N_k = 1 + 3 Pe^{0.65}$
	Wrapped foil matrix	Laminar: $f_D = \frac{96}{Re}$ Turbulent: $f_D = 0.121 \left(\frac{\varepsilon}{d_h} + \frac{68}{Re} \right)^{0.25}$	Laminar: $Nu = 8.23$ Turbulent: $Nu = 0.025 Re^{0.79} Pr^{0.33}$	Laminar: $N_k = 1$ Turbulent: $N_k = 0.022 Re^{0.75} Pr$

Cylinder	$f_D = 0$	$\text{Re}(Nu) = \begin{cases} \sqrt{2V_a Pr} & \text{if } R_t \leq 7.7\sqrt{2V} \\ \frac{0.13R_t}{\ln\left(\frac{0.35R_t}{\sqrt{2V_a Pr}}\right)} & \text{otherwise} \end{cases}$ $\text{Im}(Nu) = \frac{\tanh\left(\frac{0.4}{a}\right)}{1 + 3a} \text{Real}(Nu)$ <p>where $a = \sqrt{\frac{R_t}{7.8V_a Pr}}$</p>	$N_k = 1 + 0.014R_t$
Tube	<p>Laminar: $f_D = \frac{64}{Re}$</p> <p>Turbulent:</p> $f_D = 0.11\left(\frac{\varepsilon}{d_h} + \frac{68}{Re}\right)^{0.25}$	<p>Laminar steady:</p> $Nu = 6$ <p>Turbulent:</p> $Nu = 0.036Re^{0.8}\left(\frac{l}{d_h}\right)^{-0.055}Pr^{0.33}$	<p>Laminar:</p> $N_k = 1$ <p>Turbulent:</p> $N_k = 0.022Re^{0.75}Pr$

The solution method for the governing equations of Eqs. (14)-(17) are as follows. The gas-dynamic equations are discretized over a grid of points (x_j, t_j) uniformly spaced throughout the domain and over the cycle period. Upon this grid, variables ρ , ρuA and ρe are solved implicitly or interpolated explicitly according to the logic of a staggered-grid formulation. The essential idea is to solve ρuA at alternate nodes from ρe and ρ to avoid solution instability and produce global conservation of mass, momentum and energy: ρuA is solved at the control volume boundaries, while ρ and ρe are solved at the midpoints. The entire domain comprises an integral number of control volumes. Global conservation of energy and mass automatically hold for the solved variables ρ and ρe if one is careful to use first-order central differencing in the continuity and energy equations so that, in effect, quantities leaving one control volume enter the adjacent one [32].

The Sage program has been widely used for modeling and optimizing various thermoacoustic cryocoolers [33,34], thermoacoustic refrigerators [35], pulse tube coolers [36-38], and Stirling refrigerators [39] and engines [40]. Previous experimental validation of the models in the program showed reasonable accuracies against experimental data. For example, in a looped travelling-wave thermoacoustically-driven cryocooler by Xu *et al.* [18], the deviations between simulations and experiments for the cooling power were in the range of 5 to 15%. Likewise, deviations from the model efficiencies in Guo *et al.*'s work on a Stirling refrigerator were within 10% [41]. Simulations of a Stirling pulse tube cryocooler by Abolghasemi *et al.* showed relative deviations for the pressure drops across the cold head were within 5% of experiment [42]. The discrepancies between the Sage model and experiments mainly arise from the one-dimensional formulation, the underestimated loss from acoustic streaming, and uncertainty about the turbulence flow. Nevertheless, all the work described above show that the simulations of efficiencies are within engineering accuracy.

A two-stage thermoacoustic cooler with a piston [31] has been used to further validate the simulation model for the present work. The system to be validated includes two thermoacoustic cooler units connected by a piston and a linear compressor that provides input acoustic power. This system includes the main components of the heat exchanger, regenerator, pulse tube and piston that are similar to the proposed system, which therefore allows validation of the components required for the present model. Figure 6 illustrates the experimental and simulated cooling power under different cooling temperatures in the two-stage piston-coupled thermoacoustic cooler. The results show reasonable agreements between the experiments and the simulations in both trends and quantities. Most of the deviations in the cooling power are within 8 %: for the cooling temperature of 150 K, the averaged deviation is 4.1 %; for the cooling temperature of 130 K, the averaged deviation is 7.5 %. The largest deviation lies below 12% when the cooling temperature is 150 K. This verification illustrates that similar experimental results can be effectively predicted by the simulation model.

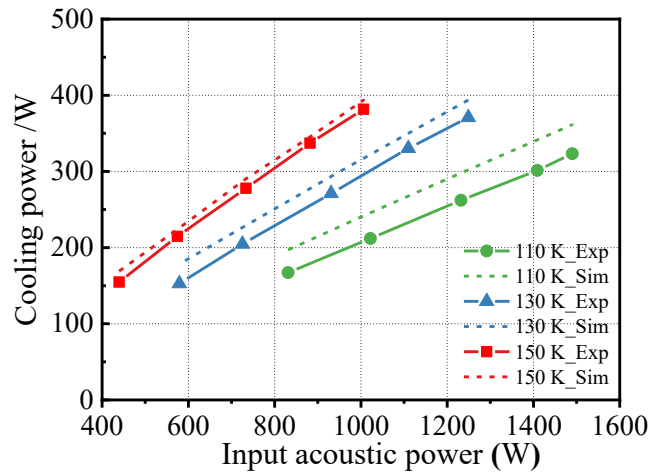


Figure 6. Experimental validation of the simulation model for the prediction of cooling capacity under different cooling temperatures in a two-stage thermoacoustic cooler with a piston. The experimental results are from Ref. [31]. Exp and Sim represent experiment and simulation, respectively.

4.2 System design method

The overall objective of the system design is to realize the maximum efficiency for each thermoacoustic unit. The direct optimization of the overall system means that each energy conversion unit may not operate at its respective optimal performance. In the present approach, the thermoacoustic energy conversion units and pistons are decoupled for the optimization. Each thermoacoustic unit is firstly optimized by changing the acoustic impedances at its two ends to achieve the highest efficiency. Then the coupled pistons are designed to match the desirable optimal acoustic impedances for each thermoacoustic unit.

Based on the individual engine and cooler unit simulations (Figure 3), the optimal values for r_e and r_c are 2.00 and 0.31, respectively, for the typical heating and cooling temperatures of 873 K and 130 K. The value of η_p is set to be 0.85 as before. Taking

these parameters, the area ratios for each thermoacoustic unit from left to right in Figure 1 are 1.0: 1.7: 2.9: 4.9: 1.3, as the area of each regenerator is approximately proportional to the generated acoustic power. The diameter of the first engine is chosen to be 60 mm, so the diameters of the second engine, third engine, first cooler and second cooler are designed to be 77, 102, 133, and 68 mm, respectively. The other component dimensions for each thermoacoustic unit are chosen to be the same as listed in Table 2.

Table 2. Component dimensions of the thermoacoustic energy conversion units

Unit	Part	Length (mm)	others
Engine	water-cooler	60	shell-tube type, 20% in porosity, 2 mm in hydraulic diameter
	regenerator	70	woven screen type, 80% in porosity, 150-mesh, 52 μm in wire diameter
	heater	80	plated-fin type, 37% in porosity, 1mm in channel width
Cooler	water-cooler	54	plated-fin type, 26% in porosity, 0.4 mm in channel width
	regenerator	74	70% in porosity, 300-mesh, 31 μm in wire diameter
	cold head	30	plated-fin type, 18% in porosity, 0.25 mm in channel width

For efficient coupling, the pistons are designed as phase shifters to achieve the optimal boundary acoustic impedances for the thermoacoustic units in terms of the highest efficiency, while keeping the dimensions and operating conditions. By optimizing the volume flow at the two ends of each thermoacoustic unit using the Sage, the simulation results of the optimal acoustic impedances are shown in Table 3.

The optimal impedances lead to the design of the coupled pistons. The force-balance equation of the piston in Eq. (21) can be written as:

$$Z_{exp} A_{exp}^2 - Z_{com} A_{com}^2 = R_m + (\omega M - K_{tot} / \omega) i \quad (25)$$

where Z is the acoustic impedance of the piston, and subscripts exp and com again refer to the expansion-side and compression-side of the piston and presented in Figure 2. Based on the force-balance equation of the piston in Eq. (25), the magnitude and phase of the acoustic impedances of the piston must be matched using:

$$|Z_{exp}| A_{exp}^2 \cos \theta_{exp} - |Z_{com}| A_{com}^2 \cos \theta_{com} = R_m \quad (26)$$

$$|Z_{exp}| A_{exp}^2 \sin \theta_{exp} - |Z_{com}| A_{com}^2 \sin \theta_{com} = \omega M - K_{tot} / \omega \quad (27)$$

In the design of the pistons, the acoustic impedances of the piston (amplitude $|Z|$ and phase θ) are chosen as the optimal values as listed on Table 3. The area A_{exp} is chosen to be the same as the area of its adjacent regenerator, the compressor frequency f is set to be a typical fixed value of 50 Hz, K_{tot} is set to be 50 kN/m which can be easily realized, R_m is chosen as approximately 500 times the expansion-side diameter based on prior experience [29], as listed on Table 3. Once $|Z_{exp}|$, θ_{exp} , $|Z_{com}|$, θ_{com} , A_{exp} , R_m , K_{tot} and ω are valued, A_{com} and M are obtained from Eqs. (26) and (27). Table 3 lists the optimal dimensions of each piston.

Table 3. Optimized acoustic impedances and dimensions of the pistons.

	1 st piston	2 nd piston	3 rd piston	4 th piston
$ Z_{exp} /\theta_{exp} \text{ ((Pa}\cdot\text{s/m}^3\text{)}/^\circ)$	$2.9 \times 10^7/34.9$	$3.1 \times 10^7/2.10$	$1.7 \times 10^7/11.1$	$1.4 \times 10^7/76.2$
$ Z_{com} /\theta_{com} \text{ ((Pa}\cdot\text{s/m}^3\text{)}/^\circ)$	$3.1 \times 10^7/-66.4$	$1.9 \times 10^7/-62.4$	$1.1 \times 10^7/-59.1$	$4.2 \times 10^7/-50.6$
D_{exp} (mm)	60	77	102	133
D_{com} (mm)	68	104	131	77
R_m ((N ² s)/m)	30.0	38.5	51.0	66.5
M (kg)	2.1	4.5	6.7	11.1
K_{tot} (N/m)	5×10^4	5×10^4	5×10^4	5×10^4

4.3 Axial distributions of key parameters

Figure 7 shows the axial distributions of the phase of the pressure and volume flow rate waves, the phase difference between the two, and acoustic power, obtained from the Sage program. The x -axis begins at the inlet of the 1st engine and ends at the outlet of the 2nd cooler. The key to achieving efficient energy conversion in a thermoacoustic system is to establish traveling-wave acoustic fields, i.e., the in-phase relationship between the pressure wave and volume flow rate, across the regenerators [23]. While the lengths of the coupled pistons are not shown in Figure 7, the key determining parameters for the phase shifting of the coupled pistons are all presented in Table 3. According to the phase difference in Figure 7 (c), the acoustic fields of the regenerators of the 1st engine ($\theta_{P_1-U_1}$ from -27.6° to 17.2°), 2nd engine ($\theta_{P_1-U_1}$ from -52.2° to -23.3°), 3rd engine ($\theta_{P_1-U_1}$ from -55.1° to -14.6°), 1st cooler ($\theta_{P_1-U_1}$ from -46.5° to 43.3°) and 2nd cooler ($\theta_{P_1-U_1}$ from -39.2° to 25.9°) are near traveling-wave fields, which result in high acoustic power and efficient energy conversion provided by each thermoacoustic unit. Furthermore, the phase differences from the left end to the right end varied from 34.9° to -67.3° for the 1st piston, 2.2° to -62.3° for the 2nd piston, 13.1° to -57.2° for the 3rd piston, and 76.7° to -51.4° for the 4th piston. These vibrations of the phase differences at two ends of each piston show that the piston plays an important role in modulating phase relationship for each thermoacoustic unit. Taking closer looks at Figure 7(a) and (b), the phase-shifting ability of each piston leads to the large phase change of the pressure wave at its two sides, while the volume flow rates at its two sides are in phase with the piston velocity.

Figure 7 (d) shows the resulting axial distribution of acoustic power. A total of 804 W acoustic power from the compressor input into the 1st engine. The acoustic power is then amplified in the 1st to 3rd engine regenerators by factors of 2.41, 2.47 and 2.46, respectively. Approximately 7225 W of the amplified acoustic power is further input into the 1st cooler, whilst the remaining 1892 W at its outlet is recovered by the 2nd cooler. Finally, 627 W of acoustic power is dissipated as heat at the inertance tube.

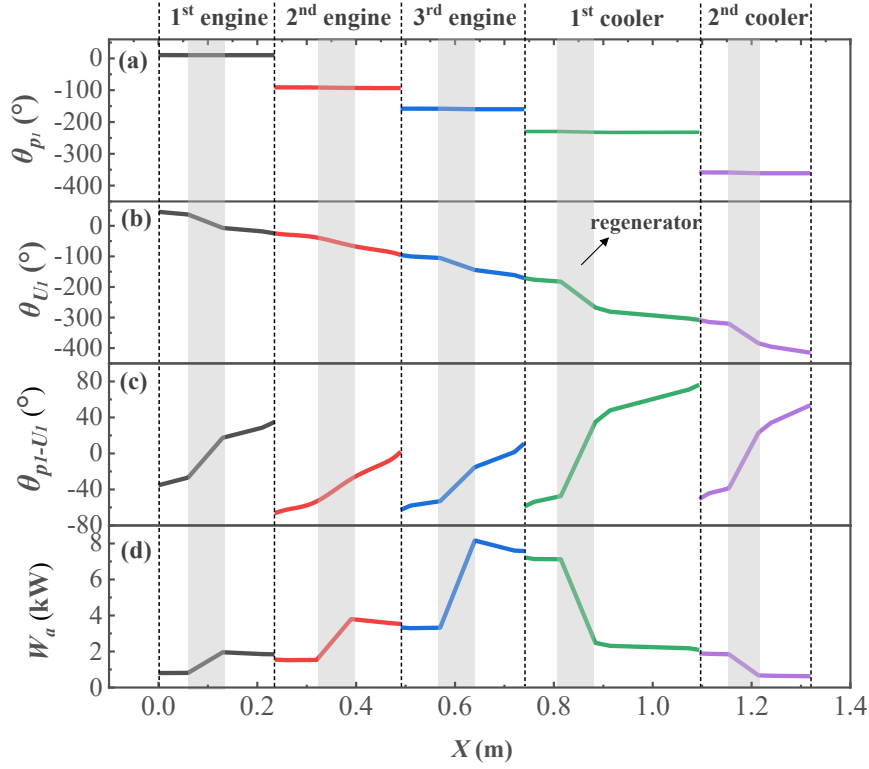


Figure 7. Axial distributions of the (a) phase of the pressure wave (b) phase of the volume flow rate (c) phase difference between the pressure wave and volume flow rate (d) acoustic power, in a system with a 3-stage engine and a 2-stage cooler. The frequency is 50 Hz, mean pressure is 35 bar, T_h is 873 K and T_c is 130 K. The lengths of the coupled pistons are not shown in the figure.

4.4 Thermodynamic performance and comparison

Table 4 presents calculation results for the system thermodynamic performance at typical working conditions. η_{eng} and η_{col} are thermal-to-cooling relative Carnot efficiencies for the multi-stage engine and cooler, respectively, where $\eta_{eng} = (W_{c,in} - W_0) / [Q_{h,all}(1 - T_0/T_h)]$ and $\eta_{col} = [Q_{c,all}(T_0/T_c - 1)] / W_{c,in}$. Under the specified operating conditions, the input thermal power increases as the number of engine stages increases: 2181 W for the 1st engine, 4006 W for the 2nd engine and 8310 W for the 3rd engine. The cooling power of 1703 W and 397 W are obtained in the 1st cooler and 2nd cooler, respectively. The system achieves $\eta_{tc,sys}$ of 23.4%, with η_{eng} of 63.5% and η_{col} of 36.8%.

Comparisons are made to two current reported highly-efficient thermoacoustically-driven coolers. One system includes three identical engine units in a loop connected by identical diameter resonance tubes, connected by a cooler unit at a branch of each unit [23]; in another system, three engine units and a cooler unit are asymmetrically connected in a loop by different diameter resonance tubes [24]. Table 4 shows the comparison of the system performance between the proposed system and the existing systems. All the results in the table are calculated using the same simulation program, where the results of the existing systems are collected from Ref. [23] and [24]. The thermal-to-cooling system efficiency $\eta_{tc,sys}$ that only considers the contributions of input thermal energy, has been selected for a fair comparison among

the heat-driven thermoacoustic coolers. The results show the proposed system can achieve much higher system efficiency compared to the existing systems. When compared to the system in Ref. [24], for example, the thermal-to-cooling efficiency is increased by a factor of over 1.6 and the cooling capacity improves by more than 1.8 for the proposed system.

Table 4. Comparison of the system performance between the proposed system and current systems. where η_{eng} and η_{col} are relative Carnot efficiency of the multi-stage engine and cooler, respectively. f is frequency, P_m is mean pressure.

System	f (Hz)	T_h/T_c (K)	P_m (bar)	$Q_{h,n}$ (W)	$Q_{c,m}$ (W)	$\eta_{eng}(\%)$	$\eta_{col}(\%)$	$\eta_{tc,sys}(\%)$
This work	50	873/130	35	1 st : 2181	1 st : 1703 2 nd : 397	63.5	36.8	23.4
				2 nd : 4006				
				3 rd : 8310				
Ref. [24]	55	923/110	70	1 st : 3051	1171	45.8	32.7	15.0
				2 nd : 5599				
				3 rd : 10440				
Ref. [23]	55	918/110	70	1 st : 7310	1 st : 390	43.1	30.3	13.0
				2 nd : 7310	2 nd : 390			
				3 rd : 7310	3 rd : 390			

4.5 Parametric sensitivity

Figure 8 presents the effects of compressor frequency, mean pressure, input power from the compressor and cooling temperature on the system efficiencies, cooling power and displacements of each piston. The input compressor power has a negligible impact on the overall efficiency, while the other parameters have significant impacts on the overall efficiency. The optimal ranges of the frequency, mean pressure and cooling temperature with respect to high efficiency are 46 to 50 Hz, 3.5 to 4.5 MPa, and 70 to 150 K, respectively. Within the estimated range of the parameters considered, sets of parameters indicate thermal-to-cooling system efficiencies above 23%. Higher mean pressure and input compressor power increase the cooling power, while increasing frequency decreases it. Higher cooling temperatures result in larger cooling power because of a smaller temperature gradient along with the regenerator. It is noted that the cooling power of the 2nd cooler accounts for a sizable 18% to 25% of the overall cooling power, thus contributing to power recovery.

The above calculation results show that the system operating characteristics are sensitive to several operating conditions, e.g. cooling temperature, mean pressure. By adjusting the input acoustic power and frequency of the compressor, the system operating under various conditions can be easily controlled. In practice, the load of the alternator may greatly vary, thereby changing the displacement of the pistons. The latter must be limited to a maximum value to prevent the breakage of springs. This can be done by reducing the input acoustic power from the compressor.

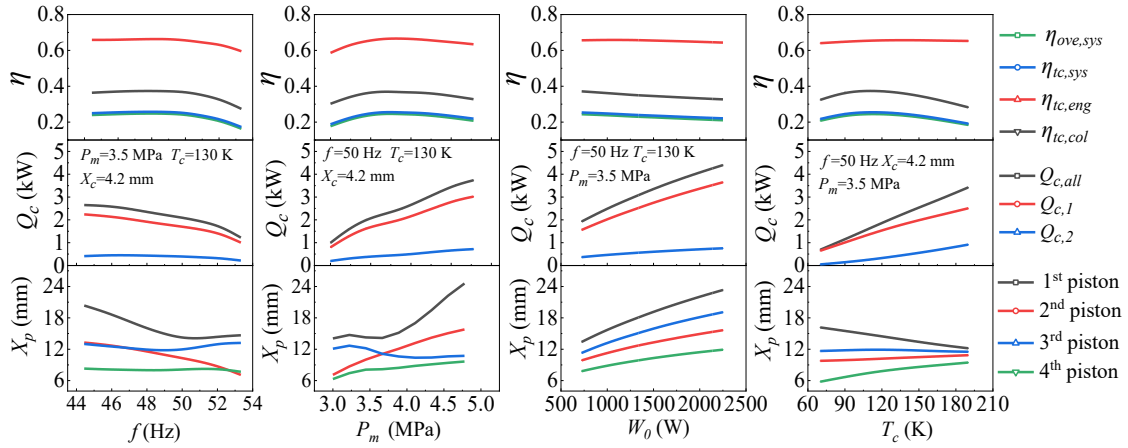


Figure 8. Dependence of the different efficiencies η , cooling power Q_c and displacement of each coupled piston X_p on compressor frequency f , mean pressure P_m , input acoustic power from the compressor W_0 , cooling temperature T_c , for a system with a 3-stage engine and a 2-stage cooler. X_c is the displacement of the compressor piston.

5. Further discussion on thermoacoustic combined cooling and power system

The above research focuses on the system that can produce cooling power while requiring external electrical power for the compressor. However, it may hinder applications where electric power is often not available. For example, significant quantities of unconventional gas are located in isolated and remote areas with a strong need to be liquefied on site. Under these conditions, it is useful to develop a heat-driven liquefaction technology without any need for external input electricity. This concept can be realized by introducing an alternator for power generation [43-45]. By replacing the cascade coolers with an alternator, the proposed system can provide combined cooling and electric power. The generated electric power can meet the demands of the compressor, obviating the need of electricity for the compressor. In this section, further discussion is made on the thermoacoustic combined cooling and power (CCP) system. Figure 9 shows the configuration of the proposed CCP system, which consists of a 3-stage engine, a 1-stage cooler, and an alternator. Figure 10 shows the key parameters of the alternator. The working principles of the overall system are as follows: the compressor provides input acoustic power to the 1st engine unit; when the axial temperature gradient along the thermoacoustic regenerator exceeds a critical value, thermoacoustic oscillation begins and the acoustic work of the pressure wave is amplified; in the subsequent engine units, the pressure wave experiences the multiple acoustic work amplification; the amplified acoustic power is then successively consumed by the cooler units; finally the remaining acoustic power is converted into electric power in the alternator. The dimensions of the thermoacoustic units and pistons are the same as those discussed in Section 4.2. Section 5.1 discusses the optimal

theoretical design of the alternator, and Section 5.2 presents system thermodynamic performance.

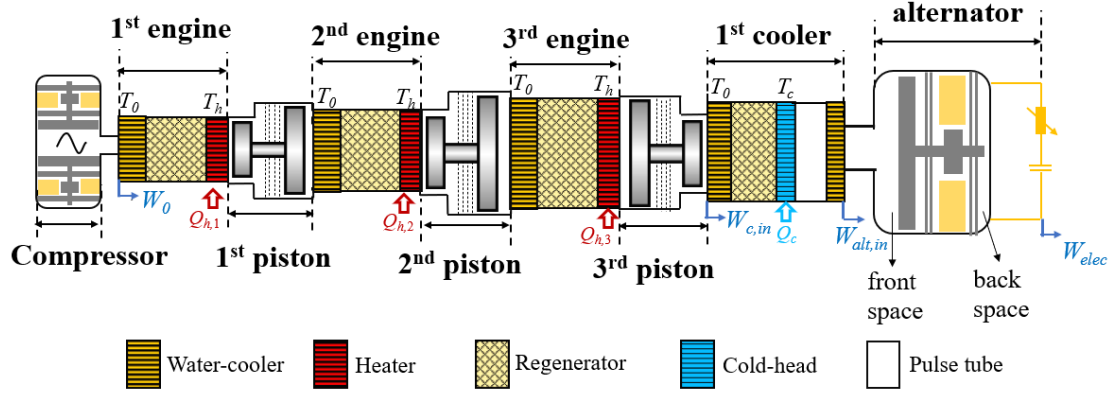


Figure 9. Schematic of the thermoacoustic combined cooling and power system.

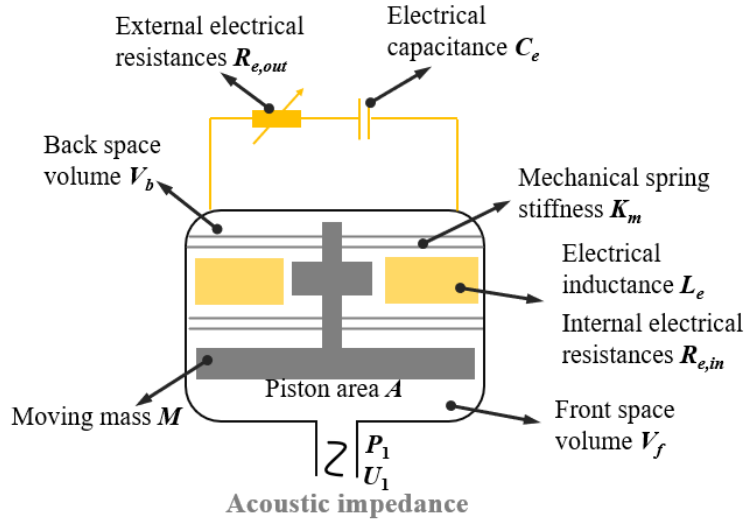


Figure 10. Key parameters of the alternator. The external electrical resistance $R_{e,out}$ and electrical capacitance C_e are connected in series outside of the alternator.

5.1 Theoretical design of the alternator

The theoretical analyses are performed to determine the optimal design of the alternator. The governing equations for an electric alternator are given by,

$$\tau \frac{U_1}{A} = I_1 (R_{e,in} + R_{e,out} + i\omega L_e) \quad (28)$$

$$\frac{\tau}{A} I_1 + \frac{R_m + i(\omega M - K_{tot} / \omega)}{A^2} U_1 = P_1 \quad (29)$$

where τ is the transduction coefficient for the alternator, U_1 is the volume flow rate, A is the area of the piston, I_1 is the electric current, $R_{e,in}$ is the internal electrical resistance, $R_{e,out}$ is the external electrical resistance, L_e is the electrical inductance, R_m is the mechanical damping of the alternator, M is the moving mass of the piston, K_{tot} is the total spring stiffness. All the above parameters are shown in Figure 10.

The acoustic impedance at the inlet of the alternator is expressed as

$$R_a + iX_a = \frac{P_1}{U_1} \quad (30)$$

By solving Eqs. (25), (26) and (28), the ratio I_1/U_1 can be expressed in terms of the acoustic impedance:

$$\frac{I_1}{U_1} = \frac{A^2 R_a - R_m + i(A^2 X_a - (\omega M - K_{tot} / \omega))}{\tau A} \quad (31)$$

The acoustic power input to the alternator, W_a , and the electric power produced by the alternator, W_e , can be calculated respectively by

$$W_a = \frac{1}{2} \text{Re}[P_1 U_1^*] = \frac{\tau}{2A} \text{Re}[U_1^* I_1] + \frac{R_m}{2A^2} |U_1|^2 \quad (32)$$

$$W_e = \frac{1}{2} \text{Re}[(I_1 R_{e,out}) I_1^*] = \frac{\tau}{2A} \text{Re}[U_1 I_1^*] - \frac{1}{2} R_{e,in} |I_1|^2 \quad (33)$$

where $\text{Re}[\]$ refers to the real part of a complex number, and the superscript * indicates complex conjugation. Taking the ratio of Eqs. (32) and (33), and substituting Eq. (31) into the equations gives the acoustic-to-electric efficiency of the alternator, η_{alt} ,

$$\eta_{alt} = \frac{W_e}{W_a} = 1 - \frac{R_m}{R_a A^2} - \frac{R_{e,in} A^2}{R_a \tau^2} \left[\left(\frac{R_m}{A^2} - R_a \right)^2 + \left(\frac{\omega M - K_{tot} / \omega}{A^2} - X_a \right)^2 \right] \quad (34)$$

where $(\omega M - K_{tot} / \omega) / A^2 - X_a = 0$, η_{alt} achieves a maximum value if all the other variables are constant. Under these conditions, the optimal moving mass M_{opt} and the alternator efficiency can be correspondingly rewritten as

$$M_{opt} = K_{tot} / \omega^2 + X_a A^2 / \omega \quad (35)$$

$$\eta_{alt} = 1 - \frac{R_m}{A^2 R_a} - \frac{R_{e,in} A^2}{\tau^2 R_a} \left(\frac{R_m}{A^2} - R_a \right)^2 \quad (36)$$

To further maximize η_{alt} , differentiating Eq. (36) with respect to A and setting the result equal to zero gives the optimum:

$$A_{opt} = \sqrt[4]{\frac{R_m^2}{R_a^2} \left(\frac{\tau^2}{R_{e,in} R_m} + 1 \right)} \quad (37)$$

$$\eta_{alt,opt} = \frac{\sqrt{\frac{\tau^2}{R_{e,in} R_m} + 1} - 1}{\sqrt{\frac{\tau^2}{R_{e,in} R_m} + 1} + 1} \quad (38)$$

Equation (38) shows that the maximum alternator efficiency only depends on the parameters of the electric alternator itself. With the parameters in Table 5 and the acoustic impedance at the expansion side of the 4th piston in Table 3, the optimal diameter and moving mass for the alternator piston is 130 mm and 12.9 kg, respectively. The corresponding maximum alternator efficiency is 85.3%.

Table 5. Main dimensions of the electric alternator. D is the diameter of the alternator piston, M is the moving mass of the alternator piston, R_m is the mechanical damping, $R_{e,in}$ is the internal electrical resistance, τ is the transduction coefficient for the alternator, K_m is the mechanical spring stiffness, L_e is the electrical inductance, V_b is the volume of the back space, and V_f is the volume of the front space, as shown in Figure 10.

D (mm)	M (kg)	R_m (kg/s)	$R_{e,in}$ (Ω)	τ (N/A)	K_m (N/m)	L_e (mH)	V_b (L)	V_f (L)
130	12.9	45	0.8	80	1.5×10^5	150	3	0.23

5.2 Simulation of system thermodynamic performance

Based on the optimized system, simulations are performed to study the system thermodynamic performance using the Sage program. In the simulation model, the constrained piston module incorporated with a damper and spring is used for the electric alternators. The multi-stage engine efficiency η_{eng} , cooler efficiency η_{col} , alternator efficiency η_{alt} , thermal-cooling-electricity system efficiency $\eta_{tce,sys}$, and overall system efficiency $\eta_{ove,sys}$ are

$$\eta_{eng} = \frac{W_{c,in} - W_0}{(Q_{h,1} + Q_{h,2} + Q_{h,3})(1 - \frac{T_0}{T_h})} \quad (39)$$

$$\eta_{col} = \frac{Q_c (\frac{T_0}{T_c} - 1)}{W_{c,in} - W_{alt,in}} \quad (40)$$

$$\eta_{alt} = \frac{W_{elec}}{W_{alt,in}} \quad (41)$$

$$\eta_{tce,sys} = \frac{\left[Q_c (\frac{T_0}{T_c} - 1) + W_{elec} \right] (1 - \frac{W_0}{W_{c,in}})}{(Q_{h,1} + Q_{h,2} + Q_{h,3})(1 - \frac{T_0}{T_h})} \quad (42)$$

$$\eta_{ove,sys} = \frac{Q_c (\frac{T_0}{T_c} - 1) + W_{elec}}{(Q_{h,1} + Q_{h,2} + Q_{h,3})(1 - \frac{T_0}{T_h}) + W_0} \quad (43)$$

where $W_{c,in}$ is the acoustic power at the inlet of the cooler unit, $W_{alt,in}$ is the acoustic power at the inlet of the alternator, as shown in Figure 9. W_{elec} is electric power obtained in the alternator.

When $\omega L_e - 1/\omega C_e = 0$, the alternator can achieve the highest acoustic-to-electric efficiency [46]. In this case, Figure 11 shows the influence of $R_{e,out}$ on the system performance at f of 50 Hz, P_m of 35 bar, T_h of 873 K and T_c of 130 K. The values of $R_{e,out}$ for the highest cooling power and the highest electric power coincide at 7.6 Ω . Table 6 presents the optimal system performance when $R_{e,out}$ is 7.6 Ω . Under the specific working conditions, the system can achieve cooling power of 1543 W and electric power of 1742 W, corresponding to $\eta_{tce,sys}$ of 33.9 % and $\eta_{ove,sys}$ of 35.6 %,

which are of course higher than the efficiencies quoted in Section 4, albeit for a lower cooling load. According to the calculation, the 1742 W of electric power generated in the alternator can well meet the energy demand of the compressor, which requires approximately 1250 W input electric power.

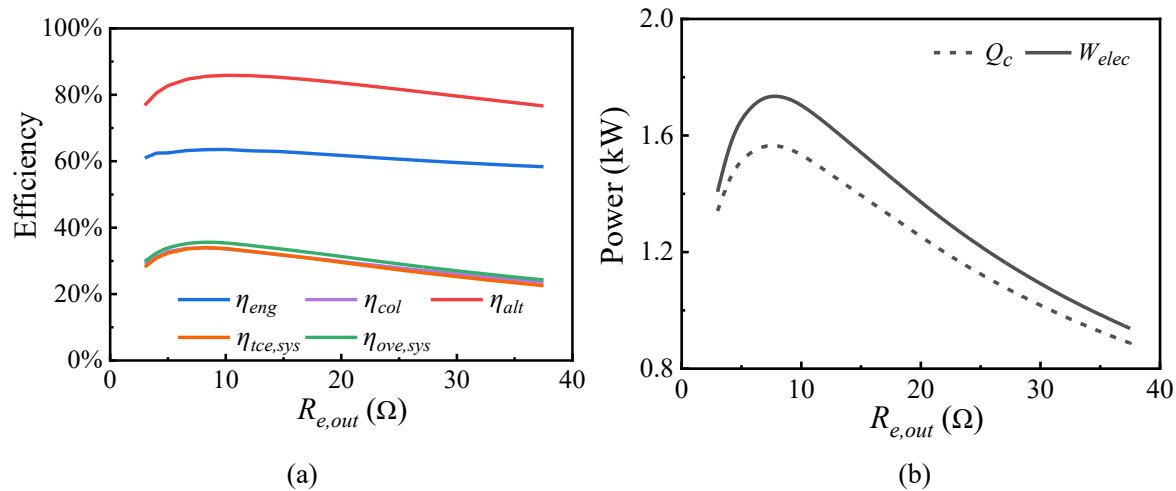


Figure 11. Influence of the external electrical resistance $R_{e,out}$ on efficiencies and power. f is 50 Hz, P_m is 35 bar, T_h is 873 K, T_c is 130 K, T_0 is 300 K, $\omega L_e - 1/\omega C_e = 0$.

Table 6. The calculated optimal performance of the thermoacoustic combined cooling and power system. $R_{e,out}$ is 7.6 Ω , and other working conditions are listed in the caption of Figure 11.

$Q_{h,n}$ (W)	$Q_{c,m}$ (W)	W_{elec} (W)	η_{eng} (%)	η_{col} (%)	η_{alt} (%)	$\eta_{ice,sys}$ (%)	$\eta_{ove,sys}$ (%)
1 st : 2086							
2 nd : 3935	1 st : 1543	1742	63.4	34.0	85.3	33.9	35.6
3 rd : 8129							

6. Conclusions

This paper proposes heat-driven coolers using intermediate coupled pistons between the thermoacoustic energy conversion units. The proposed configuration overcomes the limitations of the traditional thermoacoustic systems owing to high efficiency, compact size, and ease of control. The following conclusions can be drawn from the calculation results:

- (1) The use of multiple engine stages can cascade amplify acoustic power and overall capacity. The use of multiple cooler stages can cascade recover acoustic power, thereby improving cooling efficiency; however, in the natural gas liquefaction temperature ranges, there is no advantage in the efficiency improvement beyond two cooler stages.
- (2) The thermoacoustic units are decoupled to optimize the coupled-pistons based on the acoustic impedance matching. According to the simulation results, the optimized system achieves a thermal-to-cooling efficiency of 23% and cooling power of 2100 W at heating and cooling temperatures of 873 K and 130 K, respectively. This represents

a significant increase by a factor of more than 1.6 in efficiency as well as 1.8 in cooling capacity when compared to the existing thermoacoustic systems.

(3) The system can be operated stably under various operating conditions by using a compressor at one end of the system to actively control the input acoustic power and working frequency.

(4) A thermoacoustic combined cooling and power system is further proposed by replacing the cascaded coolers with an electric alternator. With heating and cooling temperatures of 873 K and 130 K, the system can achieve a combined cooling power of 1571 W and electric power of 1742 W, with a thermal-cooling-electricity system efficiency of 34 %. The overall system does not require any external electric power.

This work proposes a high-performance heat-driven multi-stage thermoacoustic cooler that shows great promise for future applications in, e.g., natural gas liquefaction or high-temperature superconductivity. In order for the proposed system to be successfully implemented in a variety of real-life applications, two potential problems must be considered. The first problem lies in the uncertainty of mechanical damping of the pistons, which should be determined by the available processing/assembly technique and technology level in practice. In particular, it is necessary to ensure calibration and synchronization of the work of individual sections, with regards to the non-fully controlled mechanical resistance. If the mechanical damping deviates far from the design value in practice, the system performance will be degraded. Advanced manufacturing and assembly are therefore necessary control and correct for mechanical damping. The second problem is that the load of the alternator may greatly vary in practice, thereby changing the displacement of the pistons, the control of which can be done by reducing the input acoustic power from the compressor.

Acknowledgments

This work was supported by National Natural Science Foundation of China (Grant No.51906250), National Natural Science Foundation of China (No. 51876213), and Strategic Priority Research Program of the Chinese Academy of Sciences (Grant No. XDA21080300).

References

- [1] T. Hartikainen, J. Lehtonen, R. Mikkonen. Reduction of greenhouse-gas emissions by utilization of superconductivity in electric-power generation. *Applied Energy* 2004; 78 (2):151–158.
- [2] M. Tomita, Y. Fukumoto, A. Ishihara, K. Suzuki, T. Akasaka, Y. Kobayashi, et al. Energy analysis of superconducting power transmission installed on the commercial railway line. *Energy* 2020; 209: 118318.
- [3] J.Y. Hu, E.C. Luo, L.M. Zhang, X.T. Wang, W. Dai. A double-acting

-
- thermoacoustic cryocooler for high temperature superconducting electric power grids. *Applied Energy* 2013; 112: 1166–1170.
- [4] R. Radebaugh. Cryocoolers: the state of the art and recent developments. *Journal of Physics: Condensed Matter* 2009; 21: 164219.
- [5] M.Q. Gong, J. F. Wu, Z.H. Sun, J.Y. Liu, Q. G. Hu. Development and performance test of a small trailer-mounted moveable natural gas liquefier. *Energy Conversion and Management* 2012; 57: 148–153.
- [6] X. Wang, M. Li, L. Cai, Y. Li. Propane and iso-butane pre-cooled mixed refrigerant liquefaction process for small-scale skid-mounted natural gas liquefaction. *Applied Energy* 2020; 275: 115333.
- [7] G. Chen, Y. Wang, L. Tang, K. Wang, Z. Yu. Large eddy simulation of thermally induced oscillatory flow in a thermoacoustic engine. *Applied Energy* 2020; 276: 115458.
- [8] H. Hao, C. Scalo, F. Semperlotti. Flexural-mode solid-state thermoacoustics. *Mechanical Systems and Signal Processing* 2021; 148: 107143.
- [9] R. Radebaugh, K.M. McDermott, G.W. Swift, R.A. Martin. Development of a thermoacoustically driven orifice pulse tube refrigerator. *Proceedings of the interagency meeting on cryocoolers* 1990; 205–220.
- [10] B. Arman, J.J. Wollan, G.W. Swift, S. Backhaus. Thermoacoustic natural gas liquefiers and recent developments. *Cryogenic and Refrigeration Proceedings of ICCR* 2003; 123–127.
- [11] S. Backhaus, G.W. Swift. A thermoacoustic-Stirling heat engine. *Nature* 1999; 399: 335–338.
- [12] W. Dai, E.C. Luo, J.Y. Hu, H. Ling. A heat-driven thermoacoustic cooler capable of reaching liquid nitrogen temperature. *Applied Physics Letters* 2005; 86: 224103.
- [13] R. Bao, G.B. Chen, K. Tang, W.H. Cao and T. Jin. Thermoacoustically driven pulse tube refrigeration below 80 K by introducing an acoustic pressure amplifier. *Applied physics letters* 2006; 89: 211915.
- [14] L.M. Qiu, D.M. Sun, W.L. Yan, P. Chen, Z.H. Gan, X.J. Zhang, et al. Investigation on a thermoacoustically driven pulse tube cooler working at 80 K. *Cryogenics* 2005; 45 (5): 380–385.
- [15] J.Y. Hu, E.C. Luo, W. Dai, Y. Zhou. A heat-driven thermoacoustic cryocooler capable of reaching below liquid hydrogen temperature. *Chinese Science Bulletin* 2007; 52(4): 574–576.
- [16] K. de Blok. Novel 4-stage traveling wave thermoacoustic power generator. *ASME 2010 3rd Joint US-European fluid engineering summer meeting collocated with 8th international conference on nanochannels, microchannels, and minichannels. American Society of Mechanical Engineers* 2010; 7: 73–79.
- [17] R. Yang, A. Meir, G.Z. Ramon. Theoretical performance characteristics of a travelling-wave phase-change thermoacoustic engine for low-grade heat recovery. *Applied Energy* 2020; 261; 114377.

-
- [18] K. Wang, L.M. Qiu. Numerical analysis on a four-stage looped thermoacoustic Stirling power generator for low temperature waste heat. *Energy Conversion and Management* 2017; 150 (15): 830–837.
- [19] J.Y. Xu, L.M. Zhang, J.Y. Hu, Z.H. Wu, T.J. Bi, W. Dai, et al. An efficient looped multiple-stage thermoacoustically-driven cryocooler for liquefaction and recondensation of natural gas. *Energy* 2016; 101, 427–433.
- [20] J.Y. Xu, J.Y. Hu, L.M. Zhang, E.C. Luo. A looped three-stage cascade traveling-wave thermoacoustically-driven cryocooler. *Energy* 2016; 112, 804–809.
- [21] X.Q. Zhang, J.Z. Chang, S.S. Cai, J.N. Hu. A multi-stage travelling wave thermoacoustic engine driven refrigerator and operation features for utilizing low grade energy. *Energy Conversion and Management* 2016; 114: 224–233.
- [22] K. de Blok. Multi-stage travelling wave thermoacoustic in practice. In 19th International Congress on Sound and Vibration Vilnius, Lithuania: International Institute of Acoustics and Vibration (IIAV) and Vilnius University, 2012: 1–8.
- [23] L.M. Zhang, J.Y. Hu, Z.H. Wu, E.C. Luo, J.Y. Xu, T.J. Bi. A 1 kW-class multi-stage heat-driven thermoacoustic cryocooler system operating at liquefied natural gas temperature range. *Applied Physics Letters* 2015; 107: 033905.
- [24] J.Y. Xu, J.Y. Hu, E.C. Luo, L.M. Zhang, W. Dai. A cascade-looped thermoacoustic driven cryocooler with different-diameter resonance tubes. Part I: Theoretical analysis of thermodynamic performance and characteristics. *Energy* 2019; 181: 943–953.
- [25] J.Y. Xu, J.Y. Hu, H.Z. Wang, Y.L. Sun, J.F. Hu, Z.H. Wu, et al. A cascade-looped thermoacoustic driven cryocooler with different-diameter resonance tubes. Part II: Experimental study and comparison. *Energy* 2020; 118232.
- [26] J. Chen, X. Li, Y. Dai, C. Wang. Energetic, economic, and environmental assessment of a Stirling engine based gasification CCHP system. *Applied Energy* 2021; 281: 116067.
- [27] K. Wang, S. Dubey, F.H. Choo, F. Duan. A transient one-dimensional numerical model for kinetic Stirling engine. *Applied Energy* 2016; 183: 775–790.
- [28] S. Djetel-Gothe, S. Bégot, F. Lanzetta, E. Gavignet. Design, manufacturing and testing of a Beta Stirling machine for refrigeration applications. *International Journal of Refrigeration* 2020; 115: 96–106.
- [29] J.Y. Hu, E.C. Luo, L.M. Zhang, Y.Y. Chen, Z.H. Wu, B. Gao. Analysis of a displacer-coupled multi-stage thermoacoustic-Stirling engine. *Energy* 2018; 145: 507–514.
- [30] D. Gedeon. SAGE: object-oriented software for cryocooler design. *Cryocooler* 8 1995; 281–292.
- [31] J.Y. Xu, J.Y. Hu, J. F. Hu, L.M. Zhang, E.C. Luo, B. Gao. Experimental study of a cascade pulse tube cryocooler with a displacer. *Cryogenics* 2018; 95: 69–75.
- [32] Gedeon D. Sage User's Guide, 11th ed. Athens (OH), USA: Gedeon Associate; 2016.

-
- [33] J.Y. Xu, G.Y. Yu, L.M. Zhang, W. Dai, E.C. Luo. Theoretical analysis of two coupling modes of a 300-Hz three-stage thermoacoustically driven cryocooler system at liquid nitrogen temperature range. *Applied Energy* 2017; 185: 2134–2141.
- [34] J.Y. Xu, J.Y. Hu, L.M. Zhang, W. Dai, E.C. Luo. Effect of coupling position on a looped three-stage thermoacoustically-driven pulse tube cryocooler. *Energy* 2015; 93: 994–998.
- [35] J.Y. Xu, E. Luo, S. Hochgreb. Study on a heat-driven thermoacoustic refrigerator for low-grade heat recovery. *Applied Energy* 2020; 271: 115167.
- [36] Y. Wang, Y. Cui, W. Dai, J.M. Pfotenhauer, X. Wang, E. Luo. Effects of DC flow on a cryogen-free Vuilleumier type pulse tube cryocooler. *International Journal of Refrigeration* 2020; 114: 148–154.
- [37] J.Y. Xu, J.Y. Hu, J.F. Hu, E.C. Luo, L.M. Zhang, B. Gao. Cascade pulse-tube cryocooler using a displacer for efficient work recovery. *Cryogenics* 2017; 86: 112–117.
- [38] L. Wang, M. Wu, X. Sun, Z. Gan. A cascade pulse tube cooler capable of energy recovery. *Applied Energy* 2016; 164: 572–578.
- [39] S. L. Arms, M. Gschwendtner, M. Neumaier. A novel solar-powered liquid piston Stirling refrigerator. *Applied Energy* 2018; 229: 603–613.
- [40] S. Qiu, Y. Gao, G. Rinker, K. Yanaga. Development of an advanced free-piston Stirling engine for micro combined heating and power application. *Applied Energy* 2019; 235: 987–1000.
- [41] Y. Guo, Y. Chao, B. Wang, Y. Wang, Z. Gan. A general model of Stirling refrigerators and its verification. *Energy Conversion and Management* 2019; 188: 54–65.
- [42] M.A. Abolghasemi, K. Liang, R. Stone, M. Dadd, P. Bailey. Stirling pulse tube cryocooler using an active displacer. *Cryogenics* 2018; 96: 53–61.
- [43] G. Chen, L. Tang, B. R. Mace. Modelling and analysis of a thermoacoustic-piezoelectric energy harvester. *Applied Thermal Engineering* 2019; 150: 532–544.
- [44] K. Wang, J. Zhang, N. Zhang, D. Sun, K. Luo, J. Zou, et al. Acoustic matching of a traveling-wave thermoacoustic electric generator. *Applied Thermal Engineering* 2016; 102: 272–282.
- [45] T. Bi, Z. Wu, L. Zhang, G. Yu, E. Luo, W. Dai. Development of a 5 kW traveling-wave thermoacoustic electric generator. *Applied Energy* 2017; 185: 1355–1361.
- [46] Z.H. Wu, Y.Y. Chen, W. Dai, E.C. Luo, D.H. Li. Investigation on the thermoacoustic conversion characteristic of regenerator. *Applied Energy* 2015; 152: 156–161.